

## Three-dimensional imaging of magnetic fields with polarised neutrons

Nikolay Kardjilov<sup>1\*</sup>, Ingo Manke<sup>1,2</sup>, Markus Strobl<sup>1,3</sup>, André Hilger<sup>1</sup>, Wolfgang Treimer<sup>1,4</sup>, Michael Meissner<sup>1</sup>, Thomas Krist<sup>1</sup>, John Banhart<sup>1,2</sup>

<sup>1</sup> *Hahn-Meitner Institute (HMI) Berlin, 14109 Berlin, Germany*

<sup>2</sup> *Technical University Berlin, 10623 Berlin, Germany*

<sup>3</sup> *Ruprecht Karls University Heidelberg, 69120 Heidelberg, Germany*

<sup>4</sup> *University of Applied Sciences (TFH) Berlin, 13353 Berlin, Germany*

\* *corresponding author: [kardjilov@hmi.de](mailto:kardjilov@hmi.de); Tel. +49 30 80622298; Fax. +49 30 80623059*

**Neutrons are highly sensitive to magnetic fields due to their magnetic moment while their charge neutrality allows them to penetrate even massive samples. The combination of these properties with radiographic and tomographic imaging<sup>1,2,3,4</sup> enables a technique that is unique for investigations of macroscopic magnetic phenomena inside solid materials. We introduce a new experimental method yielding two- and three-dimensional images that represent changes of the quantum-mechanical spin state of neutrons caused by magnetic fields in and around bulk objects. It opens up a way to the detection and imaging of previously inaccessible magnetic field distributions, hence closing the gap between high-resolution 2D techniques for surface magnetism<sup>5,6</sup> and scattering techniques for the investigation of bulk magnetism<sup>7,8,9</sup>. The technique was used to investigate quantum effects inside a massive lead sample that is a type-I superconductor.**

The specific interaction of neutrons with matter enables neutron radiography to complement X-ray imaging methods for analysing materials<sup>1</sup>. Conventional radiography is a geometrical projection technique based on the attenuation of a beam by a sample along a given ray. Quantum mechanically, neutrons are described by de Broglie wave packets<sup>10</sup> whose spatial extent may be large enough to produce interference effects similar to those known from visible laser light or highly brilliant synchrotron X-rays. Measurements of the neutron wave packet's phase shift induced by the interaction with matter have a long and distinguished history<sup>11,12,13,14</sup> and could recently be combined with neutron imaging approaches, where two- and even three-dimensionally resolved spatial information about the quantum mechanical interactions of neutrons with matter could be obtained<sup>2,3,15</sup>. In addition, neutrons, which from the particle physicist's point of view are small massive particles with a confinement radius of about 0.7 fm, possess another outstanding property: a magnetic moment  $\vec{\mu}$  ( $\mu = -9.66 \times 10^{-27} \text{ JT}^{-1}$ ). The

magnetic moment is anti parallel to the internal angular momentum of the neutron described by a spin  $\vec{S}$  with the quantum number  $s = 1/2$ . Consequently, the high sensitivity of neutrons to magnetic interactions has extensively been and is still being exploited in numerous experiments to study fundamental magnetic properties and to understand basic phenomena in condensed matter<sup>7,8,9</sup>.

Here, we present an experimental method that combines spin analysis with neutron imaging and yields a new contrast mechanism for neutron radiography that allows for two- and three-dimensional investigations of magnetic fields in matter. This method is unique not only for that it provides spatial information about the interaction of the spin with magnetic fields but also for the ability to measure these fields within the bulk of materials, which is not possible by any other conventional technique.

Our concept is based on the fact that any spin wave function corresponds to a definite spin direction and by using the Schrödinger equation one can keep track of the change of the spin direction during passage through an arbitrary inhomogeneous magnetic field. The equation of motion of the vector  $\vec{S}(t) = (S_x(t), S_y(t), S_z(t))$  in a magnetic field  $\vec{B}(t)$  is known to be<sup>16</sup>

$$\frac{d}{dt} S_\alpha(t) = \frac{g\mu_N}{\hbar} [\vec{S}(t) \times \vec{B}(t)]_\alpha, \quad \alpha = x, y, z, \quad (1)$$

where  $g = -3.826$  is the g-factor for neutrons, and  $\mu_N$  is the nuclear magneton. It can be shown that an ensemble of polarised particles with a magnetic moment and spin  $1/2$  behaves exactly like a classical magnetic moment<sup>17</sup>.

Thus, in a magnetic field the spin component of neutrons polarised perpendicular to the field will undergo a Larmor precession according to above equation with a frequency of

$$\omega_L = \frac{g\mu_N}{\hbar} B = \gamma_L B, \quad (2)$$

where  $\gamma_L$  is the gyromagnetic ratio of the neutron ( $-1.8324 \times 10^8 \text{ rad s}^{-1} \text{ T}^{-1}$ ) and  $B = |\vec{B}|$ .

The fundamental idea of the method presented here is to analyse the spin states in a beam after interaction with the sample for each pixel of an imaging detector and to determine spatially-resolved information about the spin rotation induced by the magnetic field of the sample<sup>4,18,19</sup>. The precession angle  $\varphi$  for a neutron traversing a magnetic field can be written as a path integral

$$\varphi = \omega_L t = \frac{\gamma_L}{v} \int_{path} B ds, \quad (3)$$

where  $v$  is the velocity of the neutron. Since the spin precession in a magnetic field depends on the flight time in the field, the incident polarised beam has to be monochromatic (i.e. has to contain neutrons with a single velocity  $v$ ). In our case the beam was monochromatised by a double reflection using two graphite crystals as monochromator.

The experimental setup as shown in Fig. 1a furthermore contains two polarisers<sup>20</sup>, one of which is situated in front of the sample position in order to define the vertical beam polarisation for the incident beam. The second polariser called (polarisation) analyser in the following is located between the sample position and the imaging detector. The analyser is aligned in parallel to the polariser in order to guarantee the passage of neutrons carrying a spin parallel to the initial polarisation and to absorb neutrons with anti parallel spin. The image of a sample detected behind the polarisation analyser is determined by a superposition of conventional attenuation contrast  $I_a(x,y)$  and the contrast variations due to spin rotation  $I_m(x,y)$

$$I(x, y) = \underbrace{I_0(x, y)}_{I_a(x, y)} \cdot \exp\left(- \int_{path} \Sigma(s) ds\right) \cdot \underbrace{\frac{1}{2}(1 + \cos \varphi(x, y))}_{I_m(x, y)} \quad (4)$$

where  $I_0(x, y)$  is the incident beam intensity,  $\Sigma$  is the linear attenuation coefficient of the sample and  $(x, y)$  are the co-ordinates in the detector plane. The cosine implies a periodic transmission function for the analysed precession angles (examples for different configurations of permanent magnets are shown as Supplementary Information in Fig. S1) and complicates a straightforward quantification with respect to the traversed magnetic fields. However, in many cases reverse approaches starting from an initial guess for the field distribution based on known symmetries, boundary conditions or reference values can be used for quantitative image analyses. Fig. 1 and 2 give examples how precisely the images can be calculated. For more complex field configurations iteration procedures help to derive the field distribution from experimental image data. In some other cases of irregular field distributions and for three-dimensional vector-field reconstructions three separate measurements of different polarisation orientations are indispensable<sup>18,19</sup>.

The experimental arrangement presented in Fig. 1a was used for recording the radiographic projection image of a dipole magnet levitating above a superconducting  $\text{YBa}_2\text{Cu}_3\text{O}_7$  pellet cooled down to 60 K (below its  $T_c = 90$  K) due to the Meissner effect (see Supplementary Information, Fig. S2 and Movie 1 for examples). The result shown in Fig. 1b illustrates the decay of the magnetic field strength with increasing distance from the magnet, resulting in an annular structure around the sample with an increasing period due to the varying precession angles of the neutron spins on their paths through the decaying field. The spatial resolution limit of the setup (see "Methods") is the reason why the annular structure cannot be resolved around the centre of the image. With respect to the regular structure of the magnetic field the dipole has been oriented parallel to the beam direction. The three-dimensional field of a dipole and the

corresponding spin rotation according to the measurement can be calculated, Fig. 1 c., (see Supplementary Information, Fig. S3a, b, for details). Comparing the measurement with the calculated data in Fig. 1d, an experimental error of about 3 % can be determined which is most likely caused by the limited precision of the energy selection and the dipole orientation with respect to the beam.

Figure 2 displays a quantitative comparison between radiographic images of an electric coil serving as an adjustable reference sample and images calculated by using Biot-Savart's law. The coil, 88 windings of aluminium wire (1 mm) wound on an aluminium rod with 10 mm diameter and a length of 108 mm, was placed perpendicular to the incident beam between the polariser and the analyser. The current was varied from 0 A up to 5 A in steps of 0.1 A, and for each step an image was recorded. The measured magnetic field in the centre of the coil was 1.0 mT for an applied current of 1 A. A reference image of the field-free sample, representing  $I_a(x,y)$ , was recorded and used to normalise the images by calculating the ratio  $I(x,y)/I_a(x,y)$ . In this way, information about the changes of the spin states, i.e. spin rotation, was extracted. These values – Fig. 2a – are compared with data derived from the calculated local magnetic field strength – Fig. 2b – and agree well with each other (see Supplementary Information, Fig. S4 and Movie 2 for more examples).

The technique was also applied to study flux trapping effects<sup>21,22,23</sup> in lead – a type-I superconductor. The sample, a polycrystalline lead cylinder, was cooled down to  $T_0=6.8$  K (below the critical temperature for superconductivity,  $T_c=7.2$  K). During cooling a homogenous magnetic field of 10 mT in parallel to the cylinder axis and perpendicular to the magnetic moment of the incident neutron beam was applied. After this, the magnetic field was switched off. Magnetic fields are partially trapped in the superconductor due to grain boundaries and other defects<sup>21,22</sup>. The temperature dependence of the residual field distribution inside the sample was visualised by

recording radiographic images during step heating from  $T_0$  to  $T_c$  with  $\Delta T=0.1$  K. The images (Fig. 3a) show an inhomogeneous residual field which decreases during heating and vanishes completely when the critical temperature  $T_c$  is reached at which superconductivity breaks down. For the case (shown in Fig. 3a – 7.0 K) of a weak trapped residual field, a tomographic investigation was performed by rotating the sample around the vertical axis, see Fig. 3b. The measurement consisted of 60 radiographic images recorded at equidistant projection angles over a range of  $180^\circ$ . The beam attenuation for each pixel can be related to equation (4) assuming that the trapped magnetic field conserves its main orientation perpendicular to the beam polarisation and is weak enough to cause spin rotations smaller than  $\pi$  for all recorded projections. For the reconstruction of the volumetric data set from the collected two-dimensional images a numerical reconstruction algorithm (filtered backprojection) was applied<sup>24</sup> resulting in a three-dimensional representation of the flux trapped in the sample at 7.0 K (Fig. 3b). Flux concentrations could be found close to the end surfaces of the cylinder and at the position where the sample was held with a screw.

In conclusion, the introduced method of neutron polarisation imaging is superior to conventional techniques since neutrons can penetrate thick layers of matter. For the first time, fields of trapped magnetic flux in a bulk superconductor could be measured, analysed quantitatively and visualised in three-dimensions. The method presented is a major step forward not only in the field of neutron imaging but also for investigations of magnetic phenomena in condensed matter. The prospects of imaging with polarised neutrons are not limited to the physics of superconductivity but can also be applied to many other fields of science and technology. For example, effects of bulk magnetism, including magnetic domain distributions in crystals, magnetoelastic and magnetostrictive stress and strains, or even electrical current distributions in conductors (causing, e.g. the skin effect) can be addressed. Hence, we predict manifold application

of our method in all areas were information about magnetic fields in bulk materials is desirable but currently not available.

## **Methods**

### **Neutron imaging technique**

The experiments were conducted at the Hahn-Meitner Institute (HMI) using the cold neutron radiography facility (CONRAD)<sup>25</sup>. A double-crystal monochromator consisting of two adjustable C(002) crystals with a mosaic spread of 3.5° was used to choose a wavelength of  $\lambda = 0.33$  nm with a band width  $\Delta\lambda/\lambda = 0.12$ <sup>26</sup>. The flux density at the sample position for an unpolarised monochromatic beam was about  $5 \times 10^5$  neutrons  $\text{cm}^{-2}\text{s}^{-1}$ . The used 400- $\mu\text{m}$  thick scintillator screen for a neutron detection was based on a powder mixture of <sup>6</sup>Li and ZnS providing a maximum light emission at 450 nm wavelength. The light was deflected by a mirror into the 55 mm focus Nikon camera lens and was recorded by an Andor DW436N-BV CCD camera with 2048×2048 pixels, each 13.5×13.5  $\mu\text{m}^2$  large. The readout time of the chip was 2  $\mu\text{s}$ /pixel. The CCD was cooled down to -50 °C to minimise electronic noise. The spatial resolution achieved was measured using a test pattern as described elsewhere<sup>27</sup>. The obtained values were 300  $\mu\text{m}$  in the vertical and 500  $\mu\text{m}$  in the horizontal direction for a sample-to-detector distance of 50 cm. Spatial resolution was deteriorated by the polarisers and the large sample-to-detector distance and was therefore below the achievable resolution of the instrument of about 100  $\mu\text{m}$ . In order to enable the investigation of samples wider than the beam width of 15 mm, a scan technique was applied. The samples together with the detector were scanned through the beam defined by the fixed polarising benders. Exposure times of the order of 15 minutes were necessary for a single image on a scan path of 6 cm.

## **Neutron polarisation**

Both solid-state polarisers used in the experiments consisted of several 250- $\mu\text{m}$  thick bent Si wafers coated on one side with FeCo polarising supermirrors and on the other side with Gd (strong neutron absorber). They either deflect or absorb neutrons depending on their spin orientation relative to the magnetic field of two permanent magnets situated on top of and beneath the benders<sup>20</sup>. The curvature causes a displacement of 250  $\mu\text{m}$  halfway through the polariser and thus avoids straight and undeflected beam paths. The measured transmission was approximately 30 % and the beam cross-section 15 mm x 40 mm (width x height). The measured degree of polarisation was  $\geq 95$  %.

## **Cryogenic technique**

For cooling the superconductor a closed-cycle refrigerator was used that allowed for adjusting a desired temperature from room temperature down to 5 K with an accuracy of 0.01 K. Magnetic fields were generated by a cylindrical Helmholtz coil.

## **Calculation procedure**

For the comparison presented in Fig. 2 the magnetic field induced by the configuration of current elements with defined strengths and orientations has been calculated as a three-dimensional array using Biot-Savart's law. The corresponding Larmor precession of the neutron spin was determined recursively voxel by voxel along line trajectories through the field, thus yielding the orientation of the final spin direction relative to the incident polarisation. This information was converted to transmission images by assigning grey values between "white" for parallel and "black" for anti-parallel spin orientation with respect to the analyser. The calculated image was convoluted with the resolution function of the instrument, an asymmetrical Gaussian with a full width at half maximum (FWHM) corresponding to the measured resolution in the vertical and

horizontal directions. The same procedure was used to compare calculated dipole fields with the measurement presented in Fig. 1. By varying the strength of the dipole field in the calculation, the measured values could be fitted and the whole dipole field could be recovered three-dimensionally (see Supplementary Information, Fig. S3a). The results could also be verified by measuring the magnetic field of  $120 \pm 5$  mT at 4 mm distance from the surface of the dipole (due to the thickness of the probe and the experimental geometry) using a Hall probe (LakeShore 421 Gaussmeter). The fact that the sample is a dipole as well as the best orientation to simplify the quantification can easily be deduced from various images recorded earlier (see Supplementary Information, Fig. S3).

**Acknowledgements** The authors would like to thank Dr. Bella Lake for helpful comments and Dr. Dirk Wallacher for experimental support.

**Author contributions** N.K., I.M., M.S. and A.H. contributed equally to this work.

**Competing financial interests** The authors declare no competing financial interests.

Correspondence and requests for materials should be addressed to N.K. ([kardjilov@hmi.de](mailto:kardjilov@hmi.de))

## References

1. Schillinger, B., Lehmann, E., Vontobel, P. 3D neutron computed tomography: requirements and applications. *Physica B* **276**, 59-62 (2000).
2. Pfeiffer, F., Grünzweig, C., Bunk, O., Frei, G., Lehmann, E., David, C. Neutron phase imaging and tomography. *Physical Review Letters* **96**, 215505 (2006).
3. Allman, B. E., McMahon, P. J., Nugent, K. A., Paganin, D., Jacobson, D. L., Arif, M., Werner, S. A. Phase radiography with neutrons. *Nature* **408**, 158-159 (2000).
4. Treimer, W., Kardjilov, N., Feye-Treimer, U., Hilger, A., Manke, I., Strobl, M. Absorption – and phase-based imaging signals for neutron tomography, *Advances in Solid State Physics* **45**, 407–420 (2005).
5. Freeman, M. R., Choi, B. C. Advances in Magnetic Microscopy. *Science* **294**, 1484-1488 (2001).
6. Zhu, Y., de Graef, M. *Magnetic Imaging and Its Applications to Materials: vol. 36 (Experimental Methods in the Physical Sciences)* (Academic Press, London, 2000).
7. Lake, B. et al. Spins in the vortices of a high-temperature superconductor. *Science* **291**, 1759-1762 (2001).
8. Coldea, R., Tennant D. A., Habicht, K., Smeibidl, P., Wolters, C., Tylczynski, Z. Direct measurement of the spin Hamiltonian and observation of condensation of magnons in the 2D frustrated quantum magnet  $\text{Cs}_2\text{CuCl}_4$ . *Physical Review Letters* **88**, 137203 (2002).
9. Brandstätter, G., Weber, H. W., Chattopadhyay, T., Cubitt, R., Fischer, H., Wylie, M., Emel'chenko, G. A., Wiedenmann, A. Neutron diffraction by the

- flux line lattice in  $\text{YBa}_2\text{Cu}_3\text{O}_{7-\delta}$  single crystals. *Journal of Applied Crystallography* **30**, 571-574 (1997).
10. de Broglie, L. Waves and quanta. *Nature* **112**, 540 (1923).
  11. Rauch, H., Treimer, W., Bonse, U. Test of a single crystal neutron interferometer. *Physics Letters A* **47a**, 369-371 (1974).
  12. Schlenker, M., Bauspiess, W., Graeff, W., Bonse, U., and Rauch, H. Imaging of ferromagnetic domains by neutron interferometry. *Journal of Magnetism and Magnetic Materials* **15-18**, 1507-1509 (1980).
  13. Zawisky, M., Bonse, U., Dubus, F., Hradil, Z., and Rehacek, J. Neutron phase contrast tomography on isotope mixtures. *Europhysics Letters* **68**, 337-343 (2004).
  14. Rauch, H., Werner, S.A. *Neutron Interferometry* (Oxford University Press, Oxford, 2000).
  15. Treimer, W., Strobl, M., Hilger, A., Seifert, C., Feye-Treimer, U. Refraction as imaging signal for computerized neutron tomography. *Applied Physics Letters* **83**, 398-400 (2003).
  16. Williams, W. G. *Polarized Neutrons* (Oxford University Press, Oxford, 1998).
  17. Mezei, F. Neutron spin echo: A new concept in polarized thermal neutron technique. *Zeitschrift für Physik* **255**, 146-160 (1972).
  18. Badurek, G., Hochhold, M., Leeb, H. Neutron magnetic tomography – A novel technique. *Physica B* **234-236**, 1171-1173 (1997).
  19. Jericha, E., Szeywerth, R., Leeb, H., Badurek, G. Reconstruction techniques for tensorial neutron tomography. *Physica B* **397**, 159–161 (2007).
  20. Krist, Th., Kennedy, S. J., Hick, T. J., Mezei, F. New compact neutron polarizer. *Physica B* **241-243**, 82-85 (1998).

21. Gammel, P., Bishop, D. Fingerprinting vortices with smoke. *Science* **279**, 410-411 (1998).
22. Jooss, Ch., Albrecht, J., Kuhn, H., Leonhardt, S., Kronmüller, H. Magneto-optical studies of current distributions in high- $T_c$  superconductors. *Reports on Progress in Physics* **65**, 651-788 (2002).
23. Johansen, T. H., Bratsberg, H., Lothe, J. Flux-pinning-induced magnetostriction in cylindrical superconductors. *Superconductor Science and Technology* **11**, 1186-1189 (1998).
24. Herman, G.T. *Image Reconstruction from Projections: The Fundamentals of Computerized Tomography* (Academic Press, New York, 1980)
25. Hilger A., Kardjilov, N., Strobl, M., Treimer, W., Banhart, J. The new cold neutron radiography and tomography instrument CONRAD at HMI Berlin. *Physica B* **385-386**, 1213-1215 (2006).
26. Treimer, W., Strobl, M., Kardjilov, N., Hilger, A., Manke, I. Wavelength tunable device for neutron radiography and tomography. *Applied Physics Letters* **89**, 203504-6 (2006).
27. Grünzweig, C., Frei, G., Lehmann, E., Kühne, G. David, C. Highly absorbing gadolinium test device to characterize the performance of neutron imaging detector systems. *Review of Scientific Instruments* **78**, 053708-11 (2007).

## Figures

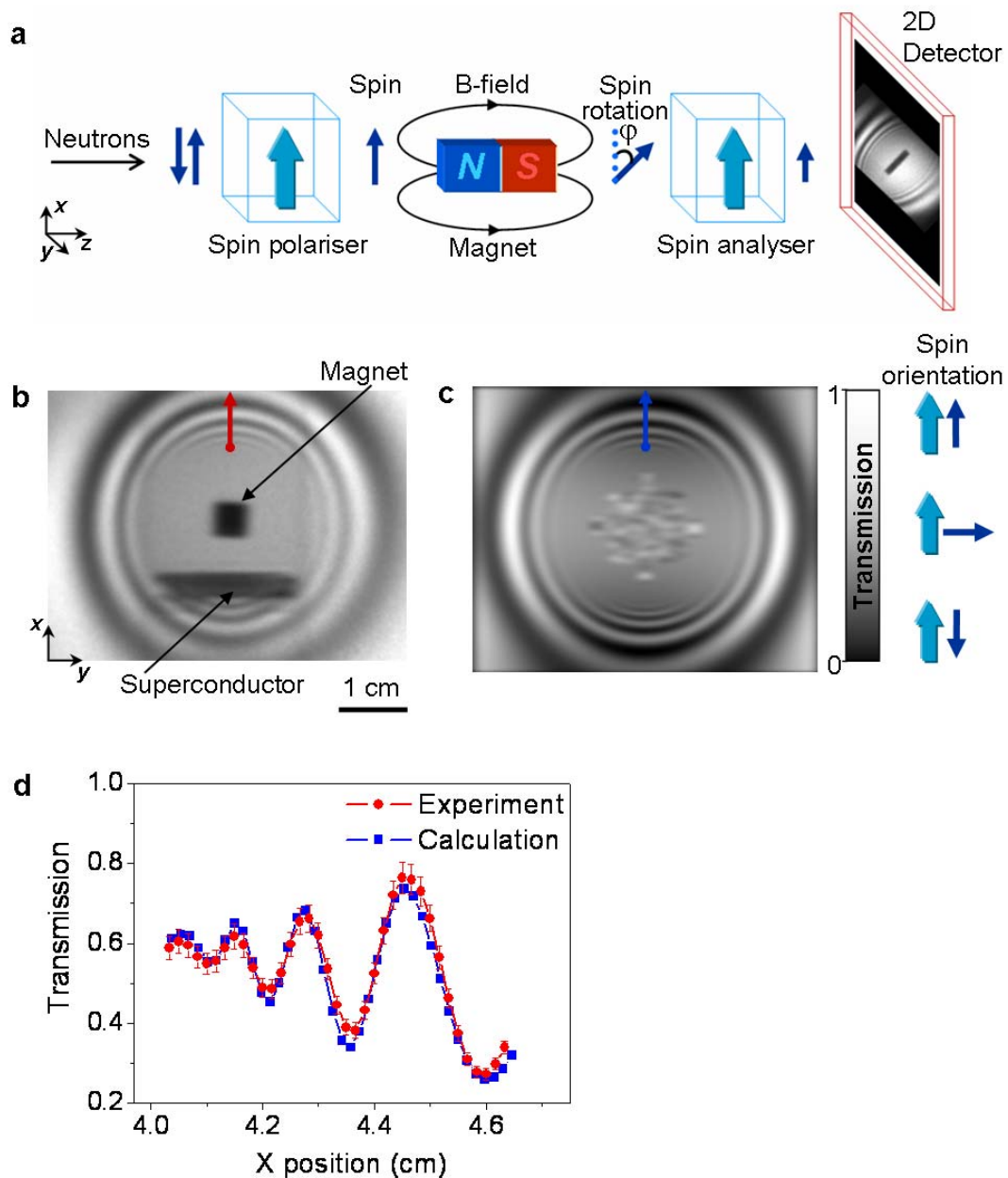


**Figure 1| Spin-polarised neutron imaging:** **a**, The neutron spin rotates in the magnetic field of a sample and hence typically approaches the spin analyser in a non-parallel orientation. The angle of the final spin rotation  $\varphi$  depends on the magnetic field along the neutron path. Changes in the polarisation alter the transmission through the polarisation analyser, which is indicated by a shorter

arrow behind the analyser. **b**, Radiogram of a permanent magnet levitating over a  $\text{YBa}_2\text{Cu}_3\text{O}_7$  superconductor obtained with spin polarised neutrons. The field of the magnet was orientated as shown in **a**. **c**, Image simulated by using the procedure described in the “Method” section. The artefact in the central part of the image is discussed in Supplement, Fig. S3b. **d**, Line profiles along the coloured arrows in **b** and **c** were used for comparison.

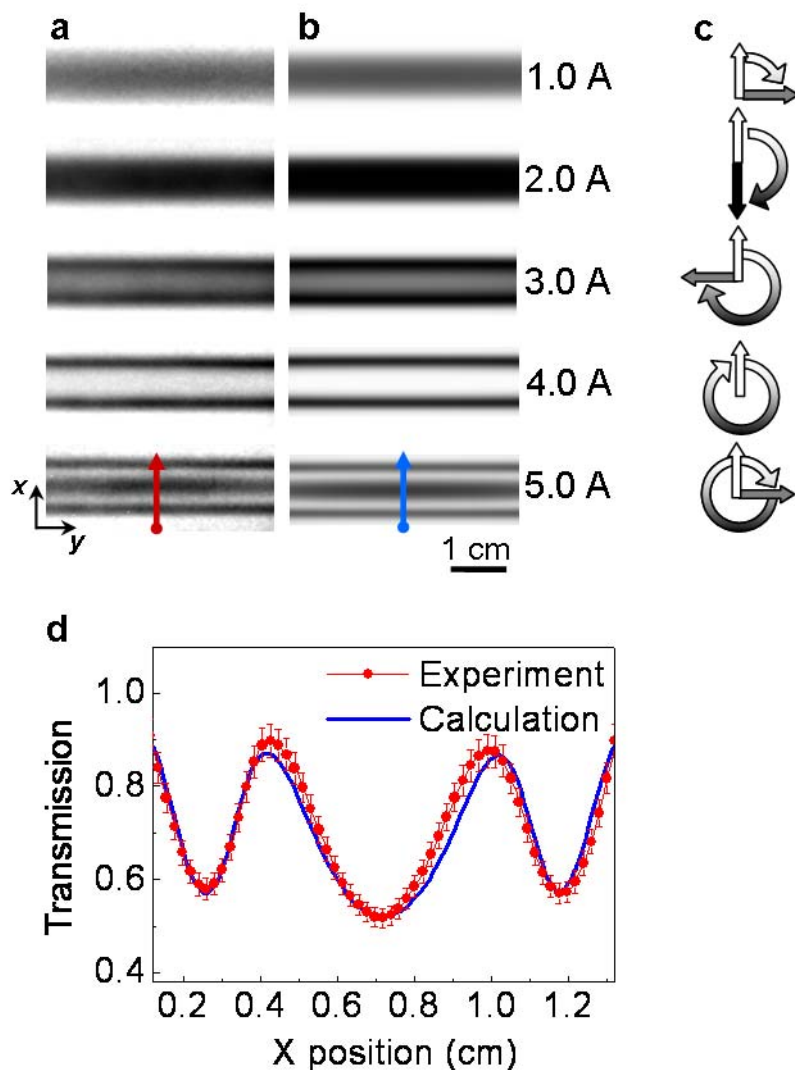


**Figure 2 | Comparison of experimental and calculated images obtained by polarised neutron radiography of a cylindrical coil driven with various currents: a**, Experimental results for five different currents. The grey scales represent the neutron spin rotation due to the magnetic field. **b**, Calculated images using Biot-Savart's law. **c**, Schematic representation of the neutron spin rotation in the image centre. **d**, Line profiles along the coloured arrows in **a** and **b** for a current 5 A. The deviation between calculation and measurement is less than 3 %.

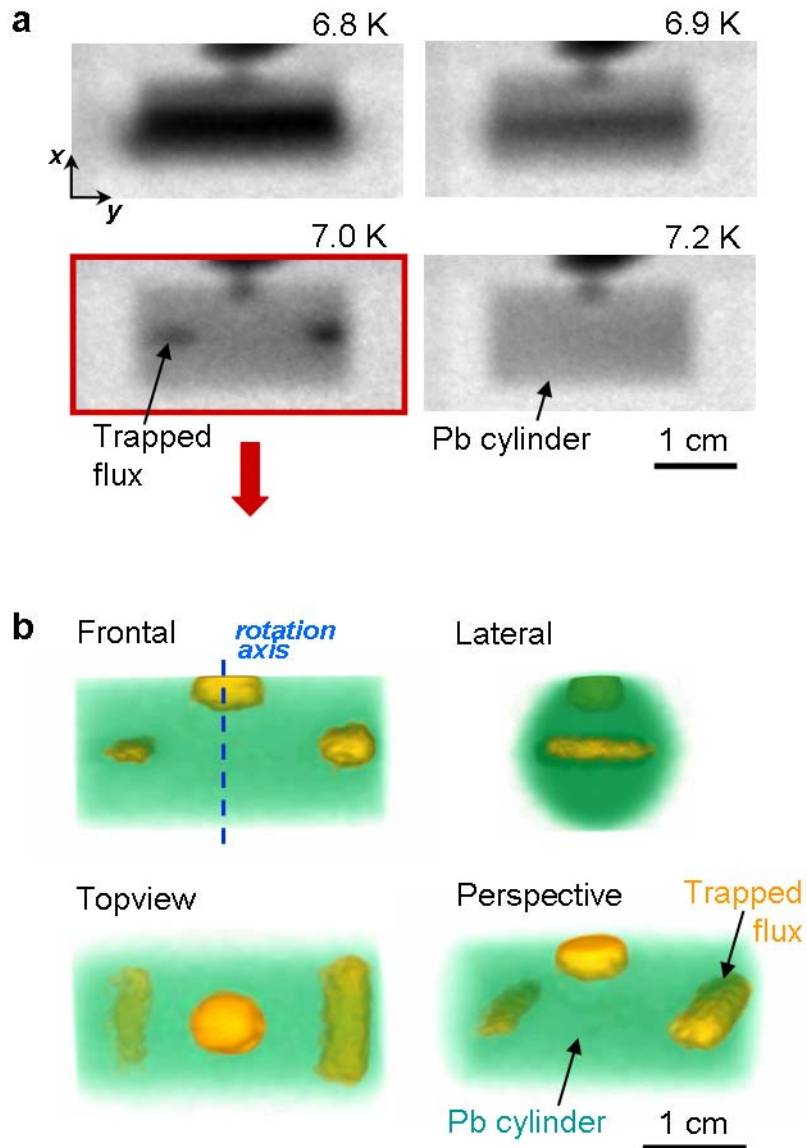


**Figure 3 | Visualisation of magnetic fields with polarised neutrons: a,** Radiographic projections of trapped flux in a polycrystalline lead cylinder at different temperatures below  $T_c = 7.2$  K. **b,** Trapped flux at 7.0 K (yellow) visualised in different tomographic views. The magnetic field strength in the sample can be analysed to be about  $1.0 \pm 0.2$  mT (yellow parts, see also Supplementary Information, Fig. S5). This result corresponds well with values observed in the reference coil in Fig. 2 which is of comparable size.

## Supplementary Information

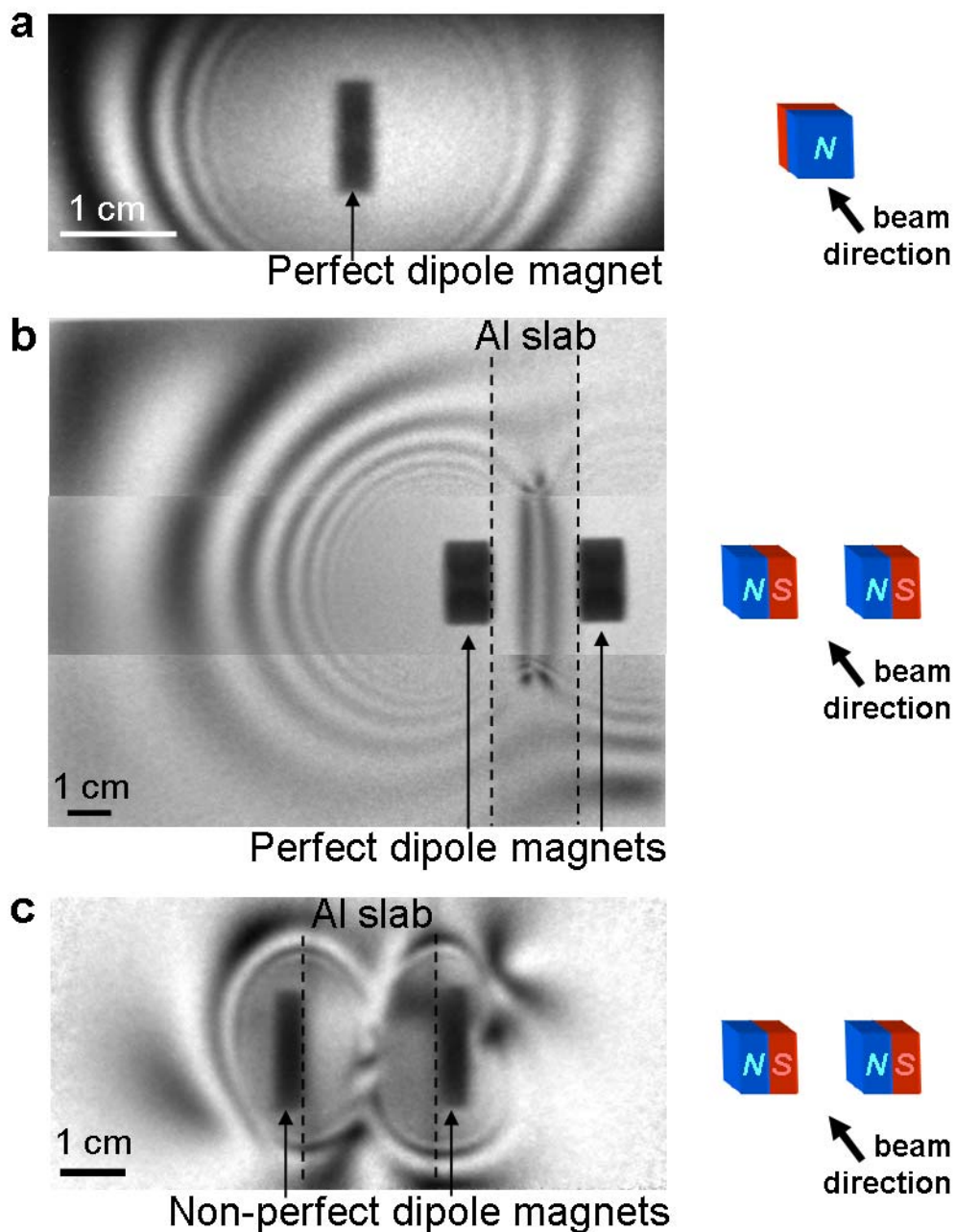


**Figure S1 | The magnetic field around different permanent magnets as visualised with spin polarised neutrons: a,** Image of a magnetic dipole. **b,** An arrangement of two magnetic dipoles was imaged (note, in order to enlarge the

field of view various images recorded independently were assembled). **c**, Image of two low-quality commercial magnets. Obviously, the magnets are not perfect dipoles but create an irregular magnetic field. In **b**, and **c**, an aluminium slab was used as a spacer between the magnets. Note that the field within the aluminium spacer slab appears as clearly as in free space.

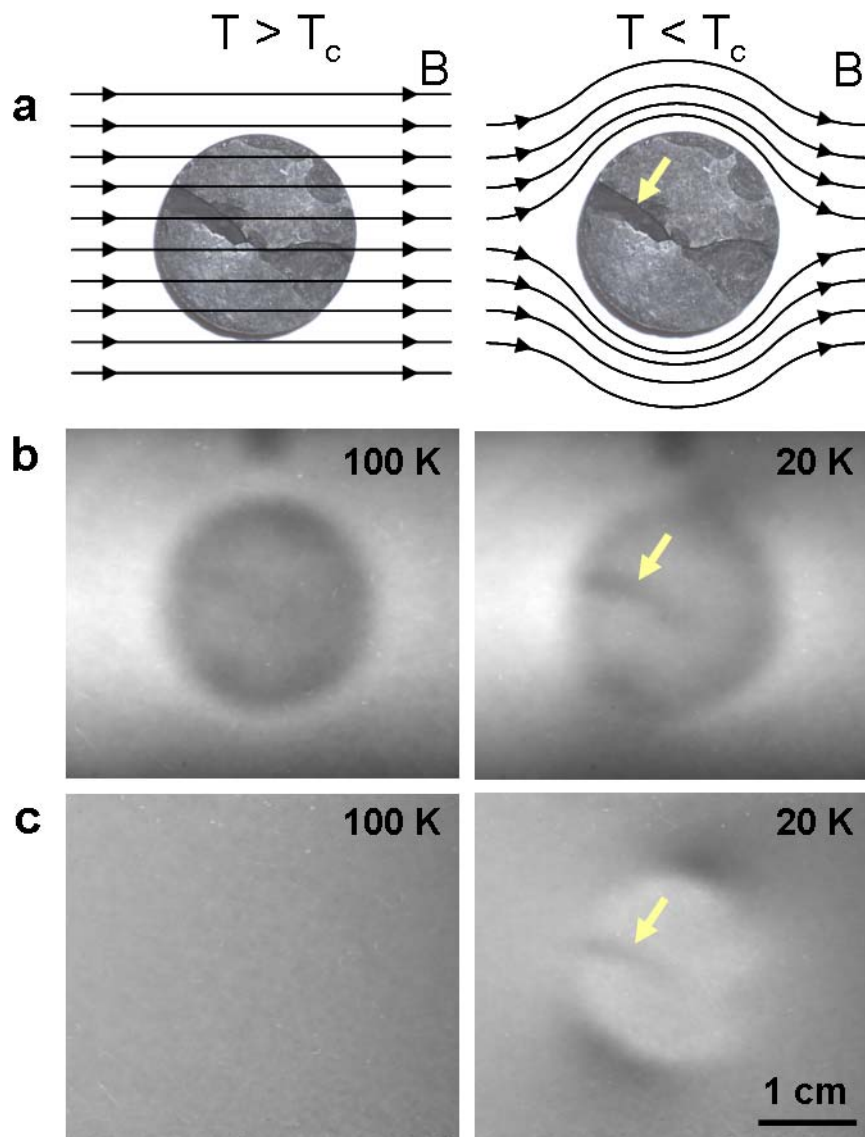


**Figure S2 | Visualisation of the Meissner effect by polarised neutron radiography:** **a**, Principle scheme of  $\vec{B}$  superimposed on an image of the investigated YBa<sub>2</sub>Cu<sub>3</sub>O<sub>7</sub> sample (a type-II superconductor). **b**, Radiographic raw images; above the superconducting temperature  $T_c = 90\text{ K}$  the magnetic field of  $0.1\text{ mT}$  can penetrate the sample and apart from attenuation a uniform polarisation over the entire sample is observed (left). Below  $T_c$  the magnetic field is squeezed out of the sample and gives rise to a different spin polarisation in the region of the sample (right). **c**, Radiographic images normalised to the

sample in zero field at 100 K. In this way the attenuation by the sample (caused by absorption and scattering) is cancelled out. For  $T = 20$  K the changes of the magnetic field modified by the expulsion from the sample becomes visible (right). The arrow marks a crack of approximately 1 mm width in the sample which could be imaged because the field was not entirely expelled in this region.

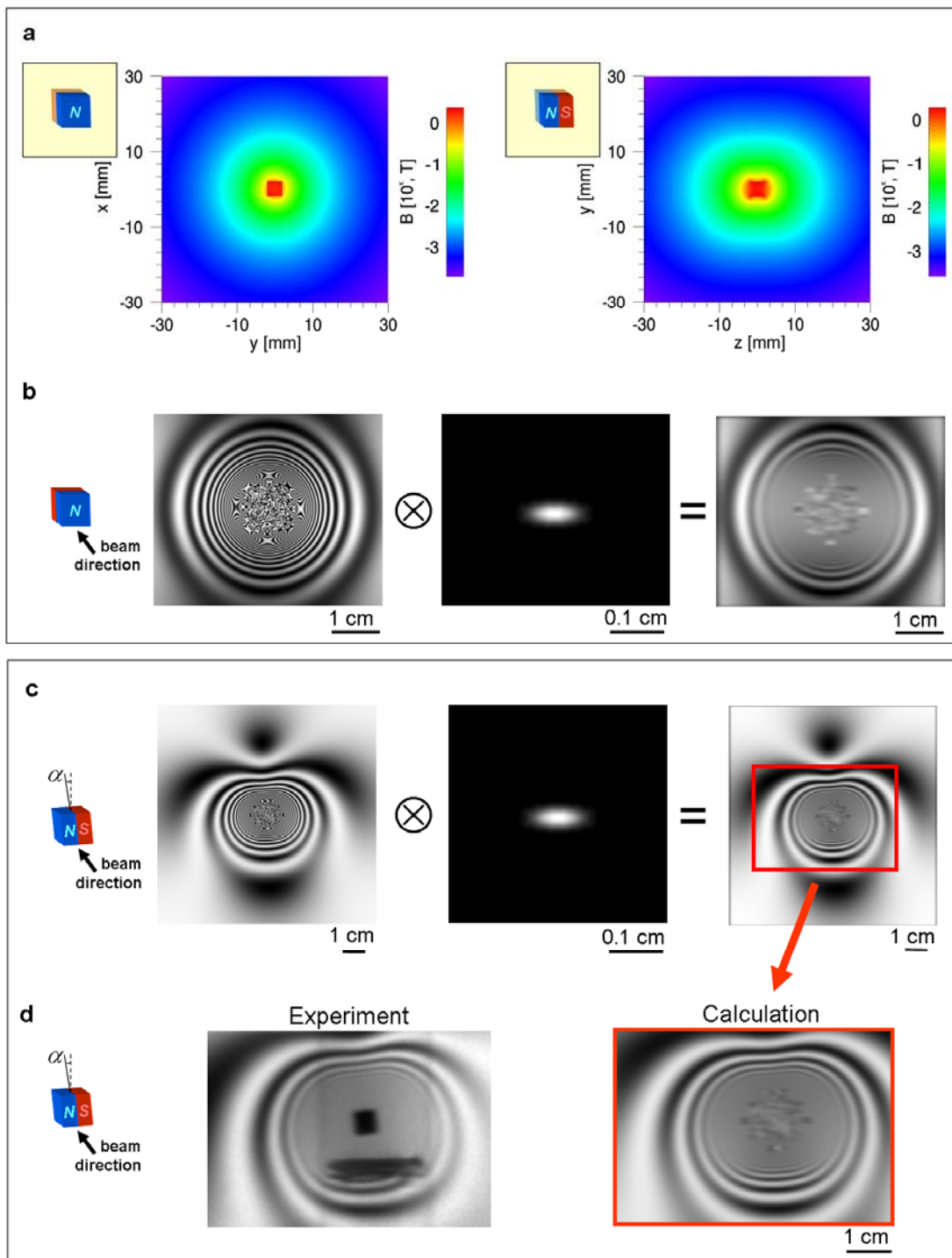


**Figure S3 | Comparison of measured and simulated spin polarised neutron radiographies of a dipole:** a, Two orthogonal slices of the three-dimensional magnetic field distribution of the levitating magnet shown in Fig 1b as retrieved by the described procedure using Biot Savart's law (see method's

section for more details). **b**, The corresponding map of the neutron spin rotation in the field was converted into a grey scale image that was convoluted with the resolution function of the instrument. For this purpose, an asymmetrical 2D Gaussian function with a horizontal FWHM of 500  $\mu\text{m}$  (in this direction the resolution is stronger influenced by the polarising bender) and a vertical FWHM of 300  $\mu\text{m}$  was used. In the central part of the image around the location of the dipole the magnetic field is very strong (up to 1.6 T), causing image artefacts due to the limited sampling of the simulation. **c**, Modified setup where the dipole was orientated perpendicular to the beam and tilted by an angle  $\alpha=4^\circ$  corresponding to the results of the image analyses. **d**, Comparison of calculation and experiment.

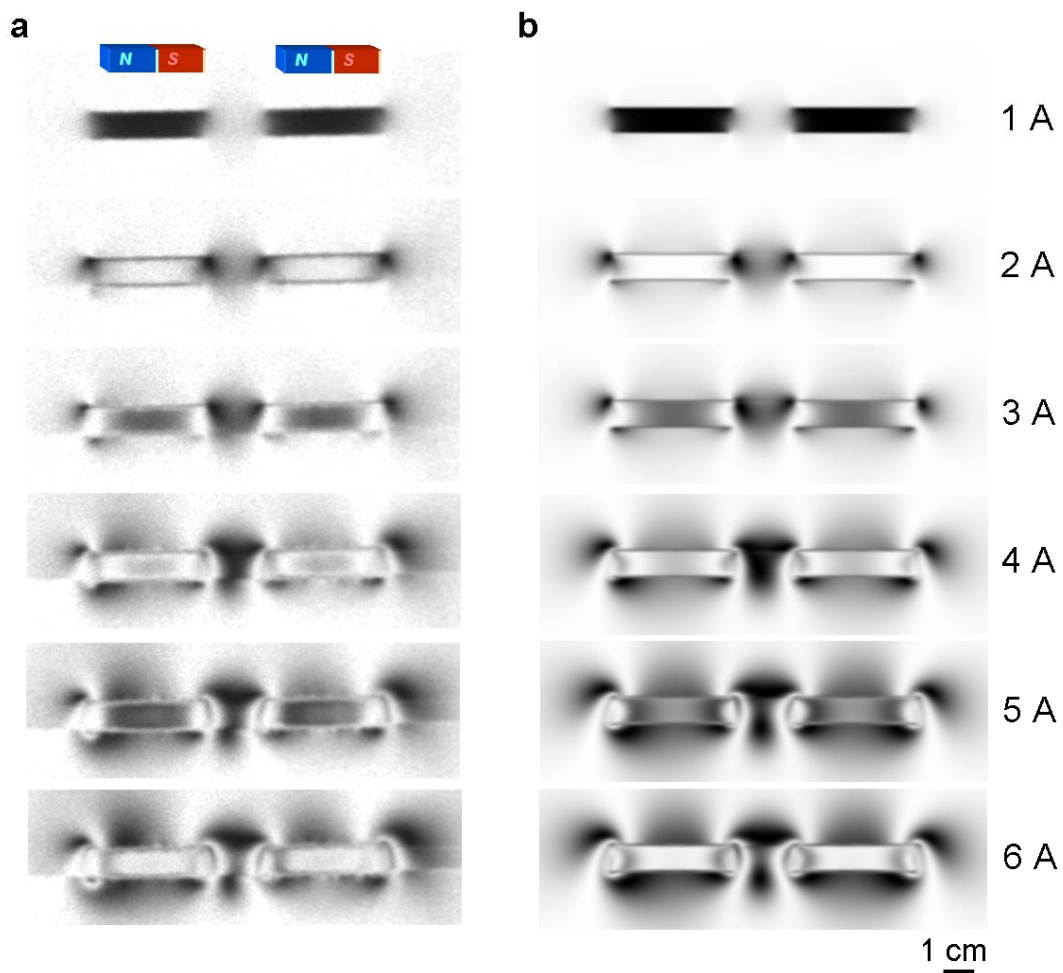


**Figure S4 | Visualisation of the magnetic field produced by a double coil:**  
**a**, Two coils with a rectangular cross section (7.5 mm x 21.5 mm) and 30 windings each (1.23 windings/mm) were arranged coaxially with a gap of 20 mm, and the magnetic field at different current values was visualised with spin polarised neutrons. **b**, Images simulated as described in the method's section. The simulated images were convoluted with the resolution function of the instrument (see Fig. S3b).

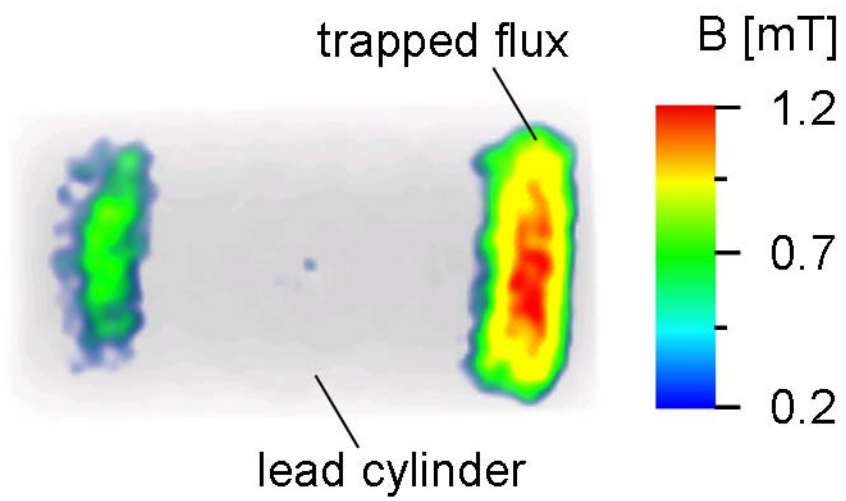


**Figure S5 | Trapped magnetic field:** Quantitative representation of the magnetic field in one slice of the tomographically reconstructed volume in Figure 3.

**Movie 1:** Observation of the Meissner effect in a cylindrical lead sample identical to that shown in Fig. 3. An inhomogeneous magnetic field was applied to the sample. As soon as the temperature decreases to below  $T_C = 7.2$  K the magnetic field is almost completely driven out of the lead sample due to its superconductivity.

**Movie 2:** Comparison between measured and simulated images shown in Fig. S4.

**Movie 3:** Distribution of the magnetic field in the lead sample shown in Fig. 3b.